Three-Dimensional Flow Visualization and Vorticity Dynamics in Revolving Wings

Authors: Bo Cheng[1], Sanjay P. Sane[2], Giovanni Barbera[1], Daniel R. Troolin[3], Tyson Strand[3] and Xinyan Deng[1*]

[1]School of Mechanical Engineering, Purdue University, West Lafayette, IN 47907, USA

[2]National Centre for Biological Sciences, Tata Institute of Fundamental Research, GKVK Campus, Bellary Road, Bangalore 560 065, India

[3]Fluid Mechanics Division, TSI Incorporated, Saint Paul, MN 55126, USA

[*]Author for correspondence (xdeng@purdue.edu; phone# 765-494-1513; fax# 765-494-0539)

Abstract

We investigated the three-dimensional vorticity dynamics of the flows generated by revolving wings using a volumetric 3-component velocimetry (V3V) system. The three-dimensional velocity and vorticity fields were represented with respect to the base axes of rotating Cartesian reference frames, and the second invariant of the velocity gradient was evaluated and used as a criterion to identify two core vortex structures. The first structure was a composite of leading, trailing and tip-edge vortices attached to the wing edges, whereas the second structure was a strong tip vortex tilted from leading-edge vortices and shed into the wake together with the vorticity generated at the tip edge. Using the fundamental vorticity equation, we evaluated the convection, stretching and tilting of vorticity in the rotating wing frame to understand the generation and evolution of vorticity. Based on these data, we propose that the vorticity generated at the leading edge is carried away by strong tangential flow into the wake and travels downwards with the induced downwash. The convection by spanwise flow is comparatively negligible. The three-dimensional flow in the wake also exhibits considerable vortex tilting and stretching. Together these data underscore the complex and interconnected vortical structures and dynamics generated by revolving wings.

1 Introduction

The flapping wings of insects operate at high angles of attack and generate strong unsteady aerodynamic and three-dimensional phenomena (Maxworthy 1981; Willmott et al. 1997; Sane 2003; Kim and Gharib 2010). Unlike conventional fixed wings which stall at high angles of attack due to instability of the vortex structures on the wing, insect wings in flapping or revolving motions are able to generate high forces and stable flows in a sustained manner throughout the duration of their motion. Recently, several studies have focused on the mechanisms that underlie the high force generation and stable vortices on flapping/revolving wings (Willmott et al. 1997; Birch and Dickinson 2001; Lentink and Dickinson 2009b).

Together these studies show that the stable attachment of a prominent leading-edge vortex (LEV) significantly enhances the lift production as compared to conventional translating wings (Ellington et al. 1996; VandenBerg and Ellington 1997; Usherwood and Ellington 2002; Birch et al. 2004). However, the mechanisms underlying the stability of the LEV have been the subject of some debate prompting researchers to use diverse experimental and theoretical approaches to address this question (e.g., Ellington et al. 1996, Birch and Dickinson 2001, Minotti, 2005, Shyy and Liu 2007). Using smoke flow visualization, Ellington and coworkers (Ellington et al. 1996) demonstrated the presence of spanwise flow within the core of a spiral LEV generated by a flapping wing at Re ~ 3000, similar to that proposed by Maxworthy (1981). They proposed that, similar to the axial flow in the vortex core of Delta wings, the spanwise transport of momentum out of the LEV was critical in keeping the LEV small but stable in flapping wings. Numerical investigations of this flow by Liu and Kawachi (1998) and Lan and Sun (2001) further detailed these phenomena. On the analytical front, Minotti (2005) used inviscid potential theory to derive a theoretical framework that demonstrated a balance between the vorticity generated by the leading edge and that transported by spanwise flow. To test the hypothesis that spanwise transport of vorticity mediated by an axial flow keeps it small and stable, Birch and coworkers (Birch and Dickinson 2001; Birch et al. 2004) placed orthogonal plates along the wing span to limit the span wise flow at Re ~ 200. They found that even under these conditions, the wing continued to generate a stable LEV. To explain this discrepancy, Birch and Dickinson proposed that strong downward flow induced by the flapping wings limits the growth of the LEV (Birch and Dickinson 2001). These results were in agreement with computational fluid dynamics-based simulations of flows under similar conditions (Shyy and Liu 2007).

To experimentally test the hypothesis that spanwise flow contributes to stabilization of the leading edge vortex, Beem et.al. (2012) used swept and translating, rather than revolving, wings to generate spanwise flows but did not observe significant differences in the time required for break-off and downstream convection of the vortex as compared to wings of lower sweep angles which generate less spanwise flow. Specifically, for cases of low sweep angles, they observed the tip vortex and the LEV as being unconnected structures with a pronounced gap region. Reminiscent of the Birch and Dickinson (2001) study, the flow induced by the tip vortex caused a pronounced downwash that prevented flow separation near the tip. For large sweep angles however, the LEV and tip vortices were more connected and inter-dependent. However, they did notice significant differences in the flow topologies of the LEV and tip vortices. These results indicated that in the swept wing case, spanwise flow may not have much influence on the LEV stabilization and attachment. To what extent do these observations apply to flapping wings? Recently, using dynamically-scaled robotic wings, Lentink and Dickinson (2009 a,b) showed that LEV stability is determined by their Rossby numbers (a ratio of inertial force to rotational accelerations, Lentink and Dickinson, 2009b), rather than Reynolds numbers (a ratio of inertial to viscous forces) which only affect the LEV integrity (Fig. 5 in Lentink and Dickinson 2009b). Using 3D flow visualization, Kim and Gharib (2010) showed that spanwise flow is widely distributed in the wake, and suggested that its generation may be attributed to the vorticity tilted from the LEV.

It is evident from the above-described research that force and flow generation by flapping wings is distinctly three-dimensional in nature, and thus traditional DPIV which can only image a plane at a time is limited in its ability to rigorously quantify such flows. Developments in the area of three-dimensional particle tracking (e.g. Troolin and Longmire 2009; Pereira et al. 2000; Kim and Gharib 2010; Flammang et al. 2011) provide the means to address the above questions relating to flows around flapping wings. Here, we used a technique called volumetric 3-component velocimetry (V3V) to quantify the three-dimensional flows around wings revolving at high angles of attack. From the velocity and vorticity fields, we identified the vortex structure from the second invariant of the velocity gradient. By calculating different terms of the vorticity equation, we also quantified the components due to vortex tilting/stretching and convection and thus account for the various terms underlying the balance of leading-edge vorticity.

2 Material and methods

2.1 Experimental setup and procedure

All experiments reported here were conducted with a dynamically scaled mechanical wing, which was inspired by nature to reproduce the flow and study the aerodynamics in natural fliers (similar setups are described in Sane, 2001, DiLeo 2007). The wing, which was capable of two-degrees-of-freedom rotations about vertical and wing longitudinal axes, was used to produce the revolving motion at a constant angular speed (Ω = 55 degs s^{-1}). The angle of attack (AOA) was fixed at 45°. Both degrees of freedom were driven by DC motors (Maxon Motor AG, Sachseln, Switzerland). The motion control system used here has been previously detailed in Zhao et al. (2009). The constant angular velocity with fixed angle of attack (AOA) meant that time-dependent effects due to wing acceleration such as added mass could be ignored as they were negligible (Dickinson et al. 1999; Sane and Dickinson 2002).

The wing and the gearbox were immersed in the center of a tank (61 × 61 × 305 cm width × height × length) filled with mineral oil (kinematic viscosity ≈ 8 cSt at 20ºC, density ≈850 kg m^3). A rectangular wing platform was used with a length of 8cm (from wing tip to center of rotation) and aspect ratio of 7 (two times wing length/mean chord length). The wing was made from a transparent polymer sheet with uniform thickness of 0.53 mm, which remained rigid during the experiments. The wing was located approximately 3 wing lengths away from the wall of the tank and therefore any wall effects were negligible according to Sane (2011).

The Reynolds number in this study (rectangular wing) was 220 using:

$$\overline{Re} = \frac{4\pi R^2}{\upsilon(AR)T} \quad (1)$$

where the characteristic velocity is the wing tip velocity ($\frac{2\pi}{T}R$) and the characteristic length is the wing mean chord length ($c = \frac{2R}{AR}$), R is the wing length, AR is wing aspect ratio, T is period of one full revolution (6.5 s), and υ is the kinematic viscosity of the fluid.

2.2 Volumetric 3-component velocimetry process

We used a flow measurement technique, known as volumetric 3-component velocimetry (V3V; TSI Inc., Shoreview, MN, USA), first described by Periera et al. (2000), to investigate the three-dimensional flow structure around revolving wings. A similar system has been used in other studies (e.g., Flammang et al. 2011). A schematic of the experimental setup can be seen in Fig. 1. We used air bubbles pumped out of a porous ceramic filter as seeding particles (Similar methods were used Birch and Dickinson 2001, and Zhao et al., 2011). Experiments were conducted after large bubbles rose to the surface leaving behind only small bubbles with an average size of 20-50 microns. Using Stokes law, this corresponds to a rise velocity of air bubbles in mineral oil of less than 0.17 mm/s (for more description, refer to Zhao et al., 2011). Pairs of sequential images were taken simultaneously by three 4 megapixel digital cameras synchronized with an Nd:YAG pulse laser illuminating the air bubbles inside the measurement volume.

The fixed coordinate frame ($\hat{\mathbf{X}}, \hat{\mathbf{Y}}, \hat{\mathbf{Z}}$) is attached to the measurement volume defined by the V3V system (Fig. 2a, b). The measurement volume, formed by the intersection of the field of view of the three cameras, was $14 \times 14 \times 10$ cm^3 along the $\hat{\mathbf{X}}$, $\hat{\mathbf{Y}}$ and $\hat{\mathbf{Z}}$ directions. This volume was sufficient to allow the entire wing to remain within the camera view over a 100° rotation. The axis of rotation was positioned at 2cm distance from the back plane of the measurement volume (Fig. 2b) to ensure that there were no laser reflections from the shaft and gearbox. A total of 10 frames, phase-locked to the wing angular position (θ), were captured, allowing consistent captures of a sequence of 10 frames equally spaced at constant Δθ=10°, for a total span of 100°. In this study, we focus only on the steady flow structures of the revolving wing. Hence, in each experiment the image capturing was triggered after one full revolution of the wing to reduce the transient phenomena due to the wing accelerating from rest (Fig. 3). The influence of the vorticity wake from the 1st revolution is considered negligible on the flow in the 2nd revolution. The 10 frames showed identical flow structure with minimal variations, by which we could conservatively assume the flow to have settled into a stable mode. However, the wake generated by the wing was not fully within the volume for some early frames; therefore, to better demonstrate the wake in the center of the volume, results from the 8th frame are shown.

Each velocity field was calculated from an *ensemble-average* of 10 separate images captured during 10 runs with identical wing motions. The particle detection, particle tracking, and velocity field interpolation were carried out using InsightV3V software (TSI Inc., Shoreview, MN, USA). The software interpolated (using Gaussian weighting based on vector distance from the grid node) the randomly distributed velocity vectors obtained from the particle tracking algorithm into a 45 × 45 × 31 rectangular mesh grid ($\Delta x = \Delta y = \Delta z =$ 3.15mm) for the three components of velocity at each frame.

The uncertainty in the instantaneous velocity fields came primarily from spatial uncertainty pertaining to accurately identifying the exact location of the particle centroids. Temporal uncertainty is negligible in comparison since the jitter in the laser pulse timing is 10ns, and the timing resolution of the synchronizer is 1ns. Spatial uncertainty results from mean-bias and RMS errors and has been shown by Pereira and Gharib (2002) to be on the order of 1% for the streamwise and spanwise velocity components and 4% for the vertical component.

2.3 Data analysis

The velocity fields thus obtained were analyzed using custom MATLAB codes (The Mathworks, Natick, MA, USA). Because the wing revolved around a fixed axis, all the quantities were calculated with respect to the base axes of a set of rotating Cartesian frames ($\hat{\mathbf{e}}_t$, $\hat{\mathbf{e}}_y$, $\hat{\mathbf{e}}_r$), rather than a single fixed Cartesian coordinate frame ($\hat{\mathbf{X}}$, $\hat{\mathbf{Y}}$, $\hat{\mathbf{Z}}$) (Fig.4). The tangential ($\hat{\mathbf{e}}_t$) and radial ($\hat{\mathbf{e}}_r$) axes in the rotating Cartesian coordinate frames depend on the azimuthal angle (ϕ) of the fluid particle being analyzed (ϕ, Fig. 4) with the vertical axis ($\hat{\mathbf{e}}_y$) kept parallel to wing rotation axis ($\hat{\mathbf{Y}}$). Note that both the fixed ($\hat{\mathbf{X}}$, $\hat{\mathbf{Y}}$, $\hat{\mathbf{Z}}$) and rotating ($\hat{\mathbf{e}}_t$, $\hat{\mathbf{e}}_y$, $\hat{\mathbf{e}}_r$) reference frames were independent of the wing position.

In the fixed Cartesian reference system, the radial vorticity generated by the wing at a given wing position may get confounded with the tangential vorticity at another wing position. This can be avoided by converting the coordinate system to a rotating Cartesian coordinate frame. The original Cartesian mesh grid and velocity field output from V3V Insight software were converted into base vectors in the rotating Cartesian coordinate frames using the rotation matrix, $\mathrm{J}(\phi)$, such that the velocity components in rotating Cartesian l (u_t, u_y, u_r) and fixed Cartesian frame (u_x, u_y, u_z) are related by:

$$\mathbf{u}(t, y, r) = \begin{pmatrix} u_t \\ u_y \\ u_r \end{pmatrix} = \mathrm{J}\mathbf{u}(x, y, z) = \mathrm{J}\begin{pmatrix} u_x \\ u_y \\ u_z \end{pmatrix} = \begin{pmatrix} \sin(\phi)\, u_x - \cos(\phi) u_z \\ u_y \\ \cos(\phi) u_x + \sin(\phi) u_z \end{pmatrix}. \tag{2}$$

The same relation also applies to other quantities (e.g., vorticity, vortex tilting and stretching).

We calculated the velocity/vorticity gradient tensor with respect to the base vectors in the rotating Cartesian frame. Using chain rule, the gradient tensor in rotating and fixed Cartesian frames are related by

$$\nabla_{(t,y,r)}\mathbf{u}(t, y, r) = \mathrm{J}\nabla_{(t,y,r)}\mathbf{u}(x, y, z) = \mathrm{J}\nabla_{(x,y,z)}\mathbf{u}(x, y, z)\mathrm{J}^{T} \tag{3}$$

where $\nabla_{(t,y,r)}$ and $\nabla_{(x,y,z)}$ represent the gradient operation in rotating and fixed Cartesian frames, respectively. $\nabla_{(t,y,r)}\mathbf{u}(t, y, r)$ is the velocity gradient tensor in rotating Cartesian frame, which is (we neglect the subscript in the rest of paper for convenience):

$$\nabla\mathbf{u}(t, y, r) = \begin{pmatrix} \frac{\partial u_t}{\partial t} & \frac{\partial u_t}{\partial y} & \frac{\partial u_t}{\partial r} \\ \frac{\partial u_y}{\partial t} & \frac{\partial u_y}{\partial y} & \frac{\partial u_y}{\partial r} \\ \frac{\partial u_r}{\partial t} & \frac{\partial u_r}{\partial y} & \frac{\partial u_r}{\partial r} \end{pmatrix} \tag{4}$$

The above relation also applies to the vorticity gradient $\nabla\boldsymbol{\omega}$. The wing orientation was determined by tracking four vertices of the wing platform and estimating their spatial locations using the calibration process developed for the particle identification.

The velocity field, vorticity distribution and vortex structure of the flow were presented by plotting the isosurface for each component of the corresponding quantity separately. Vorticity magnitude isosurfaces were plotted with three different colors (RGB: red, green and blue) indicating the magnitude of positive (red) and negative (blue) components of radial vorticity and negative (green) component of tangential vorticity. Thus, this technique offers clear visualization of both vorticity magnitude and direction within a single isosurface plot. All of the other components (e.g., vertical vorticity) were represented by black coloring.

The vortex core structure was evaluated by calculating the second invariant of the velocity gradient, or Q value, calculated using (Jeong and Hussain 1995):

$$Q = -\frac{1}{2}(\lambda_1 + \lambda_2 + \lambda_3) \tag{5}$$

where λ_1, λ_2 and λ_3 are the eigenvalues of S^2 and Ω^2, where S and Ω are the symmetric ($\frac{1}{2}(\nabla\mathbf{u} + \nabla\mathbf{u}^T)$) and antisymmetric ($\frac{1}{2}(\nabla\mathbf{u} - \nabla\mathbf{u}^T)$) part of velocity gradient tensor $\nabla\mathbf{u}$.

Results were non-dimensionalized using the following characteristic values: velocity by wing tip velocity ($\mathbf{\Omega}R$), vorticity by wing rotation vorticity ($2\mathbf{\Omega}$) and time by half period of one wing revolution ($\pi/\mathbf{\Omega}$). All dimensionless quantities are denoted by superscript $^+$.

2.4 Vorticity equation in rotating frame

The standard Navier-Stokes equation for an incompressible fluid may be given by the following pair of equations:

$$\frac{\mathrm{D}\mathbf{u}}{\mathrm{D}\tau} = -\nabla p + \upsilon\nabla^2\mathbf{u} \tag{6}$$

$$\nabla \cdot \mathbf{u} = 0, \tag{7}$$

where $\mathbf{u}$ velocity vector, τ is time, p is pressure, υ is kinematic viscosity. The vorticity equation can be derived by taking a curl of (6), which eliminates the pressure term to give,

$$\frac{\partial \boldsymbol{\omega}}{\partial \tau} = \nabla \times (\mathbf{u} \times \boldsymbol{\omega}) + \upsilon \nabla^2 \boldsymbol{\omega}, \tag{8}$$

which upon expansion gives,

$$\frac{\partial \boldsymbol{\omega}}{\partial \tau} = (\boldsymbol{\omega} \cdot \nabla)\mathbf{u} - (\mathbf{u} \cdot \nabla)\boldsymbol{\omega} + (\nabla \cdot \boldsymbol{\omega})\mathbf{u} - (\nabla \cdot \mathbf{u})\boldsymbol{\omega} + \upsilon \nabla^2 \boldsymbol{\omega} \tag{9}$$

In this equation, $\nabla \cdot \mathbf{u} = \mathbf{0}$ due to the incompressibility condition and $\nabla \cdot \boldsymbol{\omega} = 0$ because it is a divergence of a curl of velocity. Rearranging the remaining terms, we get

$$\frac{\mathrm{D}\boldsymbol{\omega}}{\mathrm{D}\tau} = \frac{\partial \boldsymbol{\omega}}{\partial \tau} + (\mathbf{u} \cdot \nabla)\boldsymbol{\omega} = (\boldsymbol{\omega} \cdot \nabla)\mathbf{u} + \upsilon \nabla^2 \boldsymbol{\omega} \tag{10}$$

In a rotational Cartesian frame,

$$\begin{aligned}
&\boldsymbol{\omega} = \boldsymbol{\omega}' + 2\boldsymbol{\Omega} \\
&\mathbf{u} = \mathbf{u}' + \boldsymbol{\Omega} \times \mathbf{r} \\
&\frac{\mathrm{D}\boldsymbol{\omega}}{\mathrm{D}\tau} = \frac{\mathrm{D}\boldsymbol{\omega}'}{\mathrm{D}\tau} + \boldsymbol{\Omega} \times \boldsymbol{\omega} \\
&\nabla^2 \boldsymbol{\omega} = \nabla^2 \boldsymbol{\omega}' \\
&\nabla = \nabla'
\end{aligned} \tag{11}$$

where the superscript ' denotes the relative quantities observed in the rotating frame, $\mathbf{r}$, is the radial vector with the length from the fluid element to the axis of rotation. Note that $\frac{\mathrm{D}\boldsymbol{\omega}}{\mathrm{D}\tau}$ and $\frac{\mathrm{D}\boldsymbol{\omega}'}{\mathrm{D}\tau}$ are the absolute and relative rate of change of vorticity ($\boldsymbol{\omega}$) observed in fixed and rotating frames, respectively. Also, it can be shown that $\boldsymbol{\Omega} \times \boldsymbol{\omega}$ is equal to $(\boldsymbol{\omega} \cdot \nabla)(\boldsymbol{\Omega} \times \mathbf{r})$. Thus, the vorticity equation in the rotating frame may be written as

$$\frac{\mathrm{D}\boldsymbol{\omega}'}{\mathrm{D}\tau} = \frac{\partial \boldsymbol{\omega}'}{\partial \tau} + (\mathbf{u}' \cdot \nabla)\boldsymbol{\omega}' = [(\boldsymbol{\omega}' + 2\boldsymbol{\Omega}) \cdot \nabla]\mathbf{u}' + \upsilon \nabla^2 \boldsymbol{\omega}', \tag{12}$$

where the rate of vorticity change in the rotational frame ($\dot{\boldsymbol{\omega}}' = \frac{\partial \boldsymbol{\omega}'}{\partial \tau}$) is equal to the summation of vorticity convection ($-(\mathbf{u}' \cdot \nabla)\boldsymbol{\omega}'$), vortex tilting and stretching ($(\boldsymbol{\omega} \cdot \nabla)\mathbf{u}'$) and vorticity diffusion ($\upsilon \nabla^2 \boldsymbol{\omega}'$). We then separated tilting and stretching components by

$$(\boldsymbol{\omega} \cdot \nabla)\mathbf{u}' = [(\boldsymbol{\omega} \cdot \nabla)\mathbf{u}']_{\perp} + [(\boldsymbol{\omega} \cdot \nabla)\mathbf{u}']_{\parallel}, \tag{13}$$

where $[(\boldsymbol{\omega} \cdot \nabla)\mathbf{u}]_{\perp}$ is the tilting component and $[(\boldsymbol{\omega} \cdot \nabla)\mathbf{u}]_{\parallel}$ is the stretching component, and subscript $\perp$ and $\parallel$ denote the projections perpendicular and parallel to the direction of vorticity. Note that, $(\boldsymbol{\omega} \cdot \nabla)\mathbf{u}'$ includes the vortex tilting and stretching due to wing rotation $2\boldsymbol{\Omega}$ and relative vorticity $\boldsymbol{\omega}'$.

Next, we looked specifically at the radial component, which describes the leading-edge (and trailing-edge) vortices generated by the revolving motion.

$$\dot{\omega}_{\mathrm{r}}' = (\boldsymbol{\omega} \cdot \nabla)\mathrm{u}_{\mathrm{r}}' - (\mathbf{u}' \cdot \nabla)\omega_{\mathrm{r}}' + \upsilon \nabla^2 \omega_{\mathrm{r}}', \tag{14}$$

where $\mathrm{u}_{\mathrm{r}}' = \mathrm{u}_{\mathrm{r}}$ and $\omega_{\mathrm{r}}' = \omega_{\mathrm{r}}$. The convection term can be expanded as

$$(\mathbf{u}' \cdot \nabla)\omega_{\mathrm{r}}' = \frac{\partial \omega_{\mathrm{r}}'}{\partial \mathrm{t}}\mathrm{u}_{\mathrm{t}}' + \frac{\partial \omega_{\mathrm{r}}'}{\partial \mathrm{y}}\mathrm{u}_{\mathrm{y}}' + \frac{\partial \omega_{\mathrm{r}}'}{\partial \mathrm{r}}\mathrm{u}_{\mathrm{r}}', \tag{15}$$

where $\mathrm{u}_{\mathrm{t}}' = \mathrm{u}_{\mathrm{t}} - 2\Omega \mathrm{r}$ and $\mathrm{u}_{\mathrm{y}}' = \mathrm{u}_{\mathrm{y}}$. Note that $\frac{\partial \omega_{\mathrm{r}}'}{\partial \mathrm{t}}\mathrm{u}_{\mathrm{t}}'$ and $\frac{\partial \omega_{\mathrm{r}}'}{\partial \mathrm{y}}\mathrm{u}_{\mathrm{y}}'$ describe the vorticity transport by tangential and vertical flow; $\frac{\partial \omega_{\mathrm{r}}'}{\partial \mathrm{r}}\mathrm{u}_{\mathrm{r}}'$ describes the transport by spanwise flow, which was acknowledged in the previous studies as the key mechanism to keep the leading-edge vortex stable (e.g., Ellington et al. 1996). Lastly, the tilting and stretching term can be expanded as

$$(\boldsymbol{\omega} \cdot \nabla)\mathrm{u}_r' = \frac{\partial \mathrm{u}_r'}{\partial \mathrm{t}}\omega_t' + \frac{\partial \mathrm{u}_r'}{\partial \mathrm{y}}\omega_y' + \frac{\partial \mathrm{u}_r'}{\partial \mathrm{r}}\omega_r' \quad (16)$$

where $\omega_t' = \omega_t$ and $\omega_y' = \omega_y - 2\Omega$. Note that $\frac{\partial \mathrm{u}_r'}{\partial \mathrm{t}}\omega_t'$ and $\frac{\partial \mathrm{u}_r'}{\partial \mathrm{y}}\omega_y'$ describe the vortex tilting from tangential and vertical components; and $\frac{\partial \mathrm{u}_r'}{\partial \mathrm{r}}\omega_r'$ describes the radial vortex stretching.

Based on the measured velocity field, all the terms in the vorticity equation described above could be evaluated. We used MATLAB for all the analysis. Derivatives of the velocity and vorticity were calculated using central differencing. No smooth rendering was applied to calculate velocity, vorticity and vortex tilting and stretching terms during post-processing. However, we did smooth the convection terms, which was subject to greater noise due to the vorticity gradient, which was magnified by ambient velocity (2Ωr) factor in the tangential direction (Eq. 15). Specifically, the convection terms at a meshgrid were smoothed out by (weighted) averaging it with the six nearest neighboring points, and the process was iterated five times.

3 Results and Discussions

3.1 Velocity and vorticity fields

The three-dimensional velocity and vorticity data is shown in Figs. 5 through 7. Figure 5 shows the spatial locations of the 2D slices represented in Figs. 6 and 7, in the context of the measurement volume. In the velocity isosurface plots (Fig. 6a-c), we represent radial components (Fig. 6a) with red (base to tip) and blue (tip to base), the tangential components (Fig. 6b) with green (direction of wing motion) and orange (opposite direction of wing motion), and vertical components (Fig. 6c) with purple (upward) and yellow (downward) colors.

Several interesting features are identified. First, the spanwise components of the flow are distributed both along the wing tip and downstream to the wake (Fig. 6a, d). The tangential flow in the direction of wing motion (Fig. 6b) is greater than other two components of the flow, and reaches maximum at approximately 80% of the wing span (Fig. 7g). A small upwash (purple) is also found along the leading edge and tip corner (Fig. 6c). Second, there is negligible spanwise flow at the leading edge towards the middle of span (Fig. 6e) or near the wing base (Fig. 6f), although it does gain some strength towards the tip and further into the wake (Fig. 6a, d, e). Third, a reverse spanwise flow is observed layered above this flow (Fig. 6a, d). The downwash, on the other hand, is distributed both below the wing surface and in the wake behind the wing.

The isosurfaces associated with individual vorticity components in the axes of the rotating Cartesian frame are shown in Fig. 7a-c. The radial vorticity (ω_r, corresponding to LEV and TEV) is generated at the wing edges and surface and extends into the wake downstream (Fig. 7a) to form two parallel vortex sheets of opposite sign. The spanwise and reverse spanwise flows are separated by a strong shear layer (negative tangential vorticity, green (Fig 7b). In comparison, positive tangential vorticity is distributed along the trailing-edge (Fig. 7d-f) and also extends somewhat into the wake, together with the negative components, forming two counter-rotating vortex sheets with a more dominant negative component. Together, the picture that emerges from these observations is similar to results obtained at Re ~3000 (modeled after the hawk moth *Manduca sexta*, Ellington et al, 1996) as well as Re ~200 (modeled after the fruit fly *Drosophila melanogaster*, Birch and Dickinson 2001). Although we saw a LEV localized at the leading edge similar to Ellington et al (1996), we did not measure significant flow through the core (Birch and Dickinson 2001). We found upward vorticity components ($+\omega_y$) near the wing tip (Fig. 7c, g), as they shed into the wake, and merged with the tangential vorticity in the tip vortex. There are also downward vorticity components ($-\omega_y$) close to the wing surface, perhaps due to the no-slip condition on the wing span.

To identify specific vortex structures, we plotted the total vorticity magnitude isosurfaces with RGB colors indicating the vorticity direction (Fig. 8). Based on the Q-value criteria for these flows, we identified the two major vortex structures on the wing (Fig 8b) which include the leading edge and trailing edge vortices and the tip vortex. The top structure consists of a combination of negative radial (LEV, blue) and negative tangential (TV, green) vorticity and extends into the wake (Fig. 8a). The bottom structure consists of positive radial (TEV, red) and positive tangential vorticity (representative color not shown in Fig. 8a). The top and bottom vortex structures connect at wing tip and form a horseshoe-like structure that is attached to the wing (represented by the dashed line in Fig. 8b, see also Liu, 2009). From the top portion of this structure, a long tube-like tip vortex structure extends tangentially into the wake. At the relatively low Reynolds number of 220, these vortex structures are coherent and stable, and do not disintegrate, unlike similar structures at higher Reynolds numbers (Lentink and Dickinson 2009). The horseshoe vortex structure (Fig. 8b) likely influences the observed tangential flow (Fig. 6b) in the wing wake; while the arc formed by LEV and TV core (Fig. 8b) likely influences the downwash (Fig. 6c).

Spanwise flow within the vortex core is thought to be critical for maintaining a stable LEV in flapping/revolving wings (e.g. Ellington et al. 1996; Lentink and Dickinson 2009). Because our experiments were conducted at a Reynolds numbers of 220, the magnitude of spanwise flow within the LEV core was small, however its magnitude was greater behind the wing, consistent with the observations of Birch et al. (2004). Thus, at these Reynolds numbers, the stability of LEV appears to not be guided by the spanwise flow within the core.

Our results show both the co-occurrence and inter-dependence of the spanwise flow and tangential vorticity in the wake, which supports the possibility that the spanwise flow is induced by the vortices. However, Lentink and Dickinson (2009b) raised another possibility that the spanwise flow behind the LEV is mediated by the centripetal acceleration through a process called centrifugal pumping. It explains the well-sustained spanwise (or radial) flow observed in rotating discs by conservation of mass. In this process, a fluid particle traveling with the spanwise flow undergoes Coriolis force supported by the viscous frictional force resulted from the tangential flow gradient (Lentink and Dickinson 2009b). Therefore, this mechanism requires a viscous region with considerable tangential velocity gradients. However, this region is not quite prominent in the current study and it may require further experiments to validate the possibility of centrifugal pumping. On the other hand, the observation of reverse spanwise flow (along negative radial axes, Fig. 6a, d) in the wake downstream clearly indicates the shed tangential vorticity should dominate other mechanisms on the cause of spanwise flow within that region.

3.2 Vortex tilting and stretching

We calculated vortex tilting and stretching using the measured flow dynamics (Eq. 13). Because the results were consistent between different frames; only 8th frame is shown here. In Fig. 9ai, bi, red regions represent a positive tilting/stretching in the radial component of vorticity, which reduces the strength of the LEV with negative radial components. As will be shown in section 3.3, the attenuation of the LEV by vortex tilting and stretching is important to the vortex dynamics.

In the tangential and vertical components, the tilting effects have a wider influence than stretching (Fig. 9aii-iii, bii-iii). In the region corresponding to LEV and TEV vortex sheet (Fig. 7a), a strong and consistent tangential tilting is observed. Leading ($-\omega_r$) and trailing edge ($+\omega_r$) vortices are tilted into negative and positive tangential vorticity (ω_t), across the two vortex sheets extended into the wake, consistent with the observation that negative tangential and negative radial vorticity combine at the LEV vortex sheet (top portion of the shell-like isosurface, Fig. 8a). In addition to the contribution of the vortex tilting to tangential vorticity components, there is also direct generation of tangential vorticity at the wing tip edge. These combine to give the net observed tangential vorticity in the shed tip vortex. Another possible source of the tangential vorticity is the spanwise flow creating positive ω_t due to the no-slip condition, as suggested by Kim and Gharib (2010).

3.3 Vorticity dynamics

To investigate the radial vorticity dynamics (LEV and TEV) in the wing rotating frame, and its effect on the stability of the vortex structures, we calculated and compared the individual terms of convection, stretching/tilting and diffusion in Eq. 14, 15 and 16. First, we found that the contribution of the convection along tangential and vertical direction to the vorticity change (Fig. 10a, b) is significant. In comparison, the contribution due to convection by spanwise flow is quite low and may be neglected as it is even smaller than the diffusion term (Fig. 11).

Together, these observations suggest that the convection by tangential flow carries away the negative radial vorticity generated at the leading edge (increase of positive radial vorticity, region 1 in Fig. 10a) and convects it into a region behind the wing (increase of negative radial vorticity, region 3 in Fig. 10a). In contrast, the downwash convects the vorticity out from this region, but brings it into a region between the LEV and the TEV vortex sheets (increase of negative radial vorticity, region 4, Fig. 10bi, ii). Because the positive radial vorticity (TEV) is convected into region 2 by the downwash and away from the wing by tangential flow, the net vorticity in this region remains mostly unaltered.

The vortex tilting and stretching terms ($(\boldsymbol{\omega} \cdot \nabla)\mathrm{u}_\mathrm{r}'$) have a smaller magnitude than the convection term (Fig. 10c) with an isosurface value lower than the one used for the convection term. In both regions 3 and 4, tilting/stretching create positive radial vorticity. In Eq. 16, the term $\frac{\partial \mathrm{u}_\mathrm{r}'}{\partial \mathrm{r}} \omega_\mathrm{r}'$, which compresses the leading edge vorticity, contributes most to the total tilting/stretching ($(\boldsymbol{\omega} \cdot \nabla)\mathrm{u}_\mathrm{r}'$). This compression (along $\hat{\mathbf{e}}_\mathrm{r}$) by the spanwise flow gradient creates positive radial vorticity and hence reduces the strength of the LEV, with a smaller contribution from the vorticity tilted from tangential vorticity ($\frac{\partial \mathrm{u}_\mathrm{r}'}{\partial \mathrm{t}} \omega_\mathrm{t}'$).

In comparison to convection and tilting/stretching, the vorticity diffusion (or dissipation) is generally negligible except at regions with very dense vorticity (Fig. 11). Even at these regions, contribution from diffusion is lower than other terms, and its effect on the overall vorticity dynamics may be ignored.

The overall phenomenon described above can thus be summarized as follows (Fig. 12): the vorticity dynamics and balance lead to discrete and coherent flow structures in the near-field and wake. The negative radial vorticity (LEV) generated at the leading edge (region 1) is first convected backward into the wake by tangential flow and then downward by vertical flow (region 3). It continues to be convected into a region between the LEV and the TEV vortex sheet (region 4), and is compressed by the gradient of spanwise flow and tilted into other components of vorticity. It should be noted here that this phenomenon applies to the flow at the majority of the wing span away from the wing tip and base edges. However, the relative magnitude of each component changes: the convection by vertical flow is significantly reduced close to the wing tip because the downwash is small in the region of the tip vortex; on the other hand, the convection by tangential flow becomes weaker close to the wing base because of the low local wing velocity (Ωr). The tilting/stretching term is most significant close to 75% of the wing span, and decreases towards the wing base and wing tip.

The experimental results described above quantify the vortex dynamics in fair detail and hence may be able to shed some insights into the mechanisms of stability of the LEV. In previous studies, there are two major hypotheses: 1) spanwise flow, within the LEV core or behind it, convects the lead-edge vorticity into the tip vortex that sheds into wake and prevents it from overgrowth (Ellington et al. 1996; VandenBerg and Ellington 1997; Lentink and Dickinson 2009b); this corresponds to the term $\frac{\partial \omega_r'}{\partial r} u_r'$ in Eq. 15. 2) downwash induced by wake vortices limits the growth by reducing the effective angle of attack (Birch and Dickinson 2001). The first hypothesis assumed that spanwise flow convects substantial vorticity into the tip vortex which is then shed into the wake, therefore balancing the new vorticity being generated. However, as shown here, at a low Reynolds number, the spanwise convection ($\frac{\partial \omega_r'}{\partial r} u_r'$) is small compared to the convection in the other two directions, and is unlikely to significantly affect the LEV strength. On the other hand, the negative radial vorticity in region 4 (Fig 10) is reduced by the compression effect (proportional to the gradient of spanwise flow, $\frac{\partial u_r'}{\partial r} \omega_r'$). Thus, our data support the second hypothesis that downwash limits the strength of the LEV by convecting it downward from the LEV vortex sheet to a region between the LEV and TEV vortex sheets, where it is compressed and tilted to other components of vorticity (e.g., tip vorticity).

4 Conclusions

Using a V3V system, we studied the velocity and vorticity fields generated by a revolving wing and evaluated the vorticity equation to interpret the vorticity dynamics. The results show a strong correlation between the velocity and the vorticity fields, implying the velocity is mostly induced by vorticity. The results also suggest strong three-dimensional phenomena of the flow, as there exists substantial vortex tilting and stretching. As one of the results, part of the radial vorticity is tilted into tangential vorticity, and shed into the wake. By comparing different terms in the vorticity equation, we found convection in tangential and vertical directions are responsible for a majority of the vorticity change, where those in the spanwise direction are negligible. In comparison, vortex tilting and stretching have a smaller effect than convection, but reduce the radial vorticity accumulated by vertical convection in a particular region.

In sum, the results in this paper advance the understandings on flapping/revolving wing aerodynamics, and are fundamental to future studies including more complex parameters (e.g., varying wing geometry, aspect ratio and angle of attack). The results and methods may also be extended from revolving to flapping wings to study and quantify the time-dependent unsteady phenomenon (e.g., interaction with the wake, effect of wing rotation and added mass effect introduced in Dickinson et al., 1999).

Acknowledgement

We thank former graduate student Zheng Hu for assistance with the V3V experiments, and Spencer Frank for the discussion on the experimental results.

References

Beem HR, Rival DE, Triantafyllou MS (2012) On the stabilization of leading-edge vortices with spanwise flow. Exp Fluids 52(2): 511-517

Birch JM, Dickinson MH (2001) Spanwise flow and the attachment of the leading-edge vortex on insect wings. Nature 412(6848): 729-733

Birch JM, Dickson WB, Dickinson MH (2004) Force production and flow structure of the leading edge vortex on flapping wings at high and low Reynolds numbers. J Exp Biol 207(7): 1063-1072

Dickinson MH, Lehmann FO, Sane SP (1999) Wing rotation and the aerodynamic basis of insect flight. *Science* 284(5422): 1954-1960

DiLeo C (2007) Development of a tandem-wing flapping micro aerial vehicle prototype and experimental mechanism. Master's Thesis, Mechancial Engineering, University of Delaware.

Ellington CP, van den Berg C, Willmott AP, Thomas ALR (1996) Leading-edge vortices in insect flight. Nature 384(6610): 626-630

Flammang, BE, Lauder GV, Troolin DR, Strand T (2011) Volumetric imaging of shark tail hydrodynamics reveals a three-dimensional dual-ring vortex wake structure. Proc R Soc B 278: 3670-3678

Gharib M, Pereira F (2002) Defocusing digital particle image velocimetry and the three-dimensional characterization of two-phase flows. Meas Sci Technol: 13 683-694

Jeong J, Hussain F (1995) On the identification of a Vortex. J Fluid Mech 285: 69-94

Kim D, Gharib M (2010) Experimental study of three-dimensional vortex structures in translating and rotating plates. Exp Fluids 49: 329-339.

Leishman JG (2006) *Principles of Helicopter Aerodynamics*, Cambridge Aerospace Series.

Lentink D, Dickinson MH (2009a) Biofluiddynamic scaling of flapping, spinning and translating fins and wings. J Exp Biol 212(16): 2691-2704.

Lentink D, Dickinson MH (2009b) Rotational accelerations stabilize leading edge vortices on revolving fly wings. J Exp Biol 212(16): 2705-2719.

Liu H (2009) Integrated modeling of insect flight: From morphology, kinematics to aerodynamics. J Comput Phys 228(2): 439-459.

Liu H, Kawachi H (1998) A Numerical Study of Insect Flight. J Comput Phys 146(1) 124 - 156.

Maxworthy T (1981) The Fluid-Dynamics of Insect Flight. Annu Rev Fluid Mech 13: 329-350.

Minotti FO (2005) Leading-edge vortex stability in insect wings. *Phys Rev E* 71.

Pereira F, Gharib M, Dabiri D, Modarress D (2000) Defocusing digital particle image velocimetry: a 3-component 3-dimensional DPIV measurement technique. Application to bubbly flows. Exp Fluids 29(suppl 1):S78–S84

Sane SP (2001) The aerodynamics of flapping wings. PhD thesis, Integrative Biology, University of California, Berkeley.

Sane SP (2003) The aerodynamics of insect flight. J Exp Biol 206(23): 4191-4208.

Sane SP (2006) Induced airflow in flying insects I. A theoretical model of the induced flow. J Exp Biol 209: 32-42.

Sane SP, Dickinson MH (2001) The control of flight force by a flapping wing: lift and drag production J Exp Biol 204(19): 2607-2626.

Sane SP, Dickinson MH (2002) The aerodynamic effects of wing rotation and a revised quasi-steady model of flapping flight. J Exp Biol 205(8): 1087-1096.

Shyy W, Liu H (2007) Flapping wings and aerodynamic lift: the role of leading-edge vortices. *AIAA J* 45(12)

Lan SL and Sun M (2001) Aerodynamic properties of a wing performing unsteady rotational motions at low Reynolds number. *Acta Mech.* 149: 135–147.

Troolin D, Longmire E (2009) Volumetric Velocity Measurements of Vortex Rings from Inclined Exits. Exp Fluids, 48(3): 409-420

Usherwood JR, Ellington CP (2002) The aerodynamics of revolving wings - I. Model hawkmoth wings. J Exp Biol 205(11): 1547-1564.

van den Berg C, Ellington CP (1997) The three-dimensional leading-edge vortex of a 'hovering' model hawkmoth. Phil. Trans. R. Soc. Lond. B 352(1351): 329-340.

Willmott AP, Ellington CP, Thomas ALR (1997) Flow visualization and unsteady aerodynamics in the flight of the hawkmoth, Manduca sexta. Phil. Trans. R. Soc. Lond. B 352(1351): 303-316.

Zhao L, Huang Q, Deng X, Sane SP (2009) Aerodynamic effects of flexibility in flapping wings. J R Soc Interface 7: 485-497.

Zhao L, Deng X and Sane SP (2011) Modulation of leading edge vorticity and aerodynamic forces in flexible flapping wings. Bioinspir. Biomim. 6(3): 036007.

Figure captions

Fig. 1. Schematic of the experimental setup showing the locations of the V3V camera, laser, robotic flapper, and the measurement volume.

Fig. 2. Schematics showing the measurement volume and the fixed coordinate frame ($\widehat{\mathbf{X}}$, $\widehat{\mathbf{Y}}$, $\widehat{\mathbf{Z}}$) (a), and schematics showing the top view of the experimental setup, measurement volume and the wing motion. The wing starts at $\widehat{\mathbf{X}}$ axis and rotates clockwise (b).

Fig. 3. Wing angular velocity profile indicating the image capture window.

Fig. 4. Rotating Cartesian coordinate system. Vectors are written in the base axes of a rotating Cartesian coordinate frame ($\hat{\mathbf{e}}_\mathbf{t}, \hat{\mathbf{e}}_\mathbf{y}, \hat{\mathbf{e}}_\mathbf{r}$). The tangential ($\hat{\mathbf{e}}_\mathbf{t}$) and radial ($\hat{\mathbf{e}}_\mathbf{t}$) axes vary with the azimuth angles ($\boldsymbol{\phi}$) of the particles (blue dot).

Fig. 5. Schematic showing the locations of slices exhibited in Figs. 6 and 7.

Fig. 6. Velocity components in the rotating Cartesian frame. Isosurfaces of (a) radial component (spanwise flow), with dimensionless isosurface value $\mathrm{u}_\mathrm{r}^+ = \pm 0.13$; (b) tangential component (transverse flow) with dimensionless isosurface value $\mathrm{u}_\mathrm{t}^+ = \pm 0.39$, (c) vertical component (up/down wash), with dimensionless isosurface value $\mathrm{u}_\mathrm{y}^+ = 0.08$ and -0.20. Chordwise slices located at (d) 80%, (e) 55%, and (f) 30% of the wing span as shown in Fig. 5. Color represents (reverse) spanwise flow and arrows represent tangential and vertical flow.

Fig. 7. Vorticity components in the rotating Cartesian frame. Isosurfaces of (a) radial component (lead-edge and trailing-edge vorticity). (b) tangential component (tip vorticity). (c) vertical component. $\omega_\mathrm{r}^+ = \omega_\mathrm{t}^+ = \omega_\mathrm{y}^+ = \pm\ 0.8$. Spanwise slices located at (d) trailing edge,

(e) 20° after the trailing edge, and (f) 40° after the trailing edge as shown in Fig. 5. Colors represent tangential vorticity and arrows represent spanwise and vertical flow. Horizontal slice (g) located as shown in Fig. 5. Color represents vertical vorticity and arrows represent tangential and spanwise flow.

Fig. 8. Isosurfaces of color-coded vorticity magnitude and vortex structure. Vorticity magnitude ($\omega^+ = 1.5$) viewed at two different angles, (ai) is looking down on the wing, while (aii) is looking up on the wing. Isosurfaces are color-coded to reflect the direction of vorticity. RGB values of the isosurface color correspond to the magnitudes of the vorticity components: trailing-edge vorticity ($+\omega_r$), red; leading-edge vorticity, ($-\omega_r$), blue and tip vorticity, ($-\omega_t$), green. (b) Vortex structure evaluated by the isosurface of Q value. $Q^+ = 0.25$. Isosurfaces are color-coded following the same rule in (a).

Fig. 9. Isosurfaces of vortex tilting and stretching in rotating Cartesian frame. (a) Vortex tilting: $(\omega \cdot \nabla u')^+_{\perp r} = (\omega \cdot \nabla u')^+_{\perp t} = (\omega \cdot \nabla u')^+_{\perp y} = \pm 3$. (ai) radial component, (aii) tangential component, (aiii) vertical component. (b) Vorticity stretching: $(\omega \cdot \nabla u')^+_{\parallel r} = (\omega \cdot \nabla u')^+_{\parallel t} = (\omega \cdot \nabla u')^+_{\parallel y} = \pm 3$, (bi) radial component, (bii) tangential component, (biii) vertical component.

Fig. 10. Isosurfaces of individual terms in vorticity equation (ai, bi and ci) and corresponding cylindrical slices at 75% of wing span (aii, bii and cii). (ai) and (aii): vorticity convection by tangential flow $\frac{\partial \omega_r'}{\partial t} u_t'$. (bi) and (bii): vorticity convection by vertical flow $\frac{\partial \omega_r'}{\partial y} u_y'$. (ci) and (cii) total vortex tilting and stretching $\omega \cdot \nabla u_r'$ The isosurfaces in (a) and (b) are shown at dimensionless value 8, and that in (c) is shown at dimensionless value 3. Regions 1, 2, 3 and 4 are indicated in both isosurfaces and cylindrical slices. In (cii), the locations for LEV and TEV are also plotted.

Fig. 11. Isosurface of diffusion term $\nabla^2 \omega_r$ and corresponding cylindrical slice. (a) isosurface shown at dimensionless value ±3. (b) Cylindrical slice at 75% of the wing span.

Fig. 12. Schematic demonstrating the vorticity dynamics. Region 1-4 are corresponding to those in Fig. 10. Blue and red arrows represent convection of negative and positive radial vorticities. A background contour of radial vorticity is also plotted to illustrate the distribution of the LEV and the TEV.

Figure1

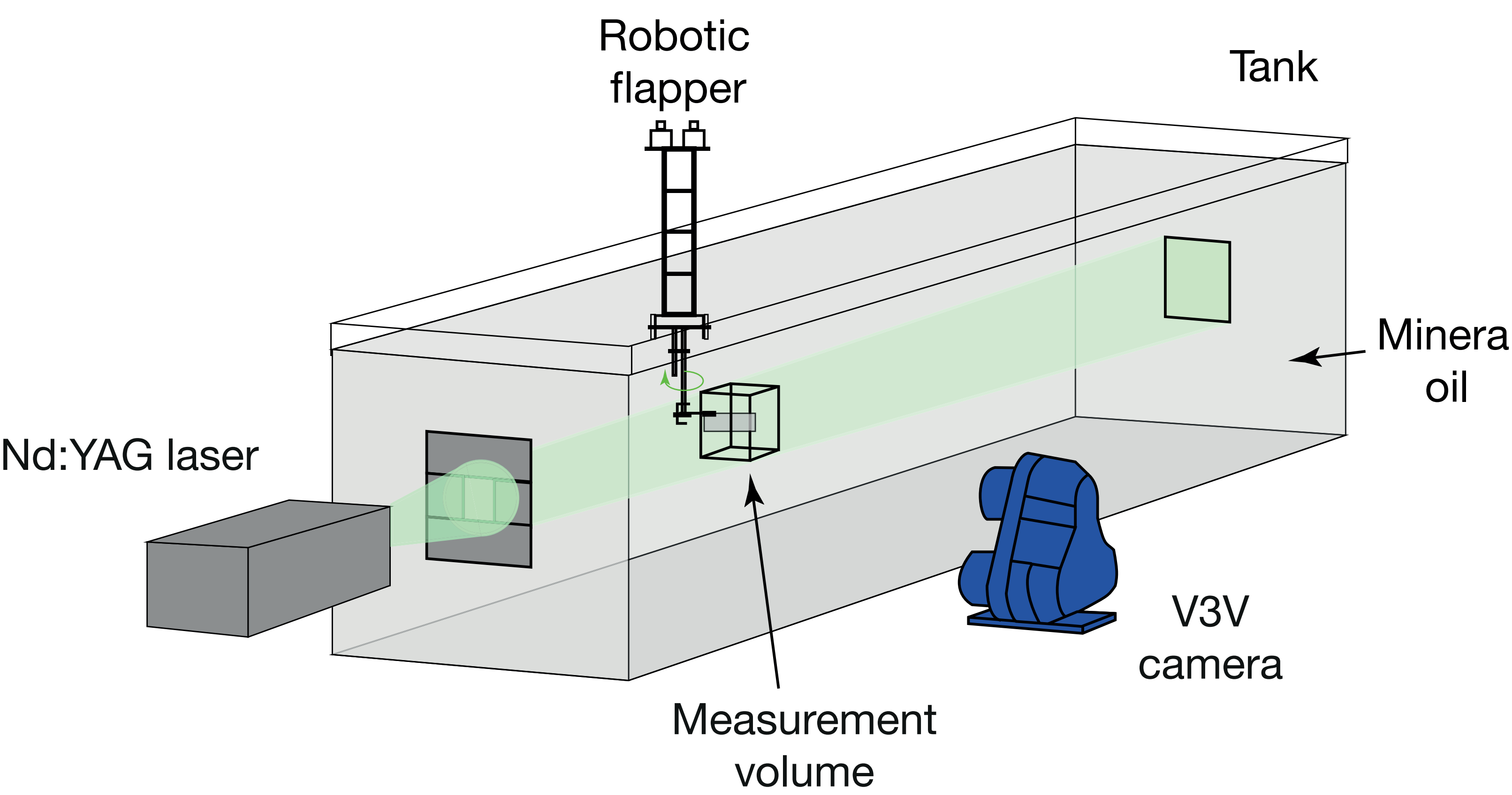

Robotic
flapper
Tank
Mineral
oil
Nd:YAG laser
V3V
camera
Measurement
volume

Figure2

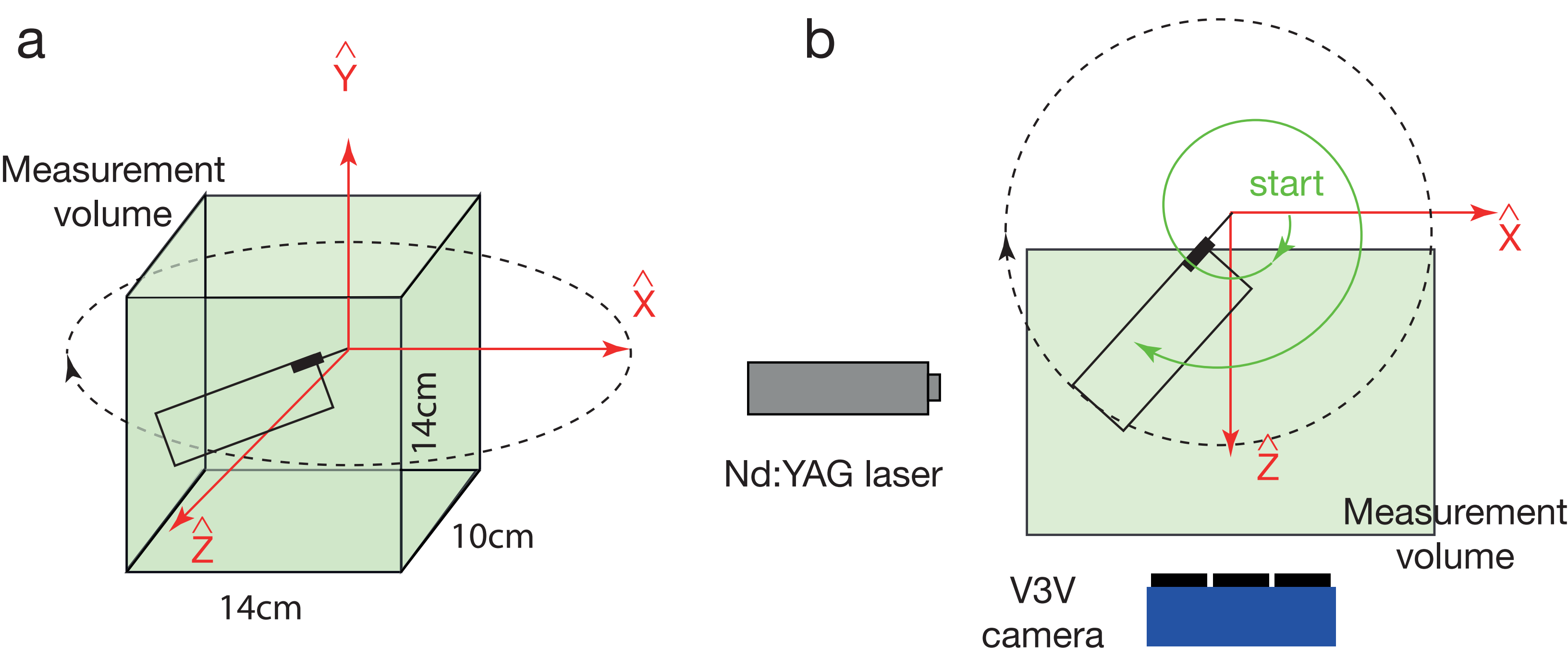
a
Ŷ
Measurement
volume
X̂
14cm
Ẑ
10cm
14cm
b
start
X̂
Nd:YAG laser
Ẑ
Measurement
volume
V3V
camera

Figure3

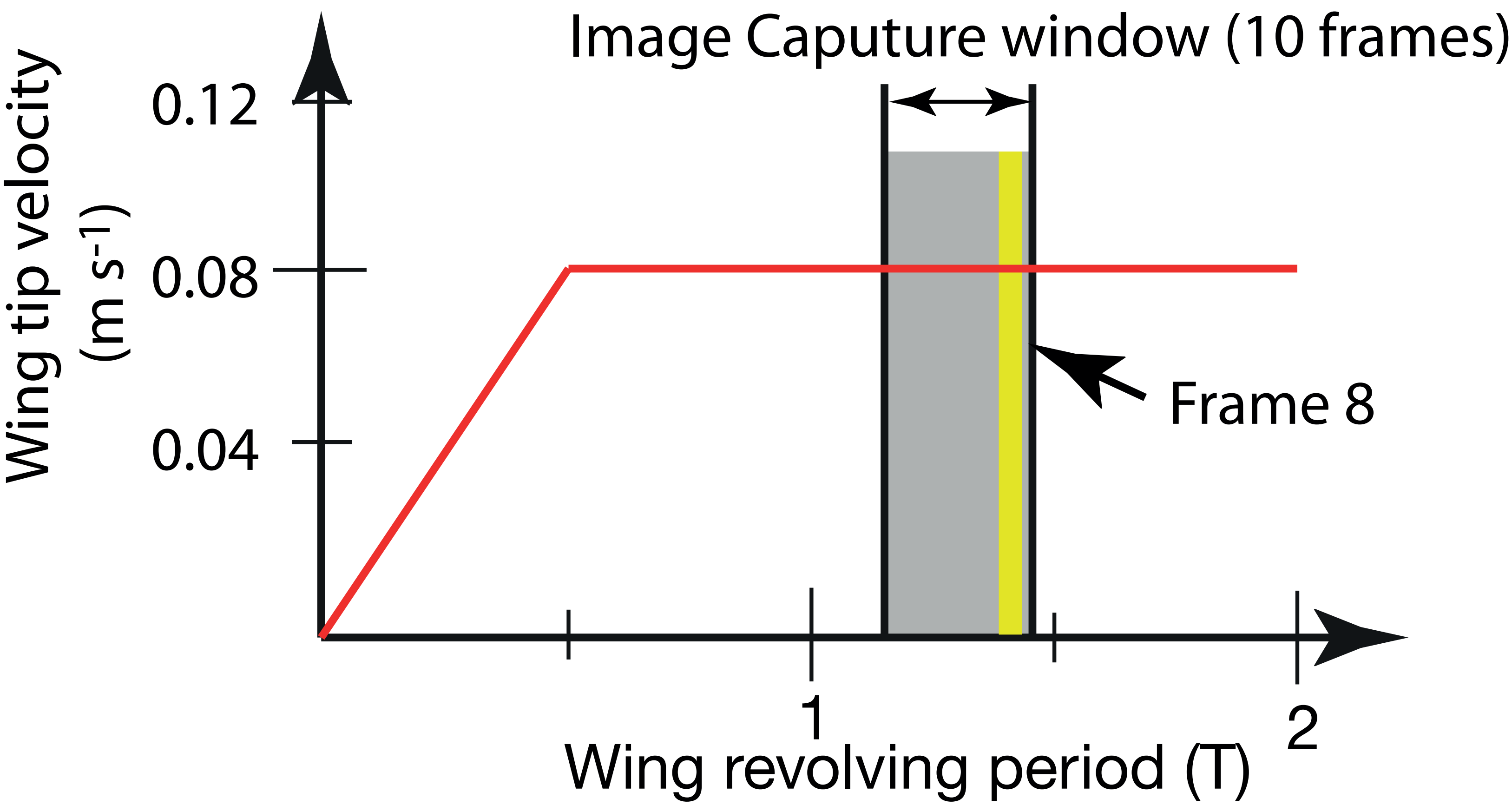

Image Caputure window (10 frames)
Wing tip velocity
(m s-1)
0.12
0.08
0.04
Frame 8
1
2
Wing revolving period (T)

Figure4

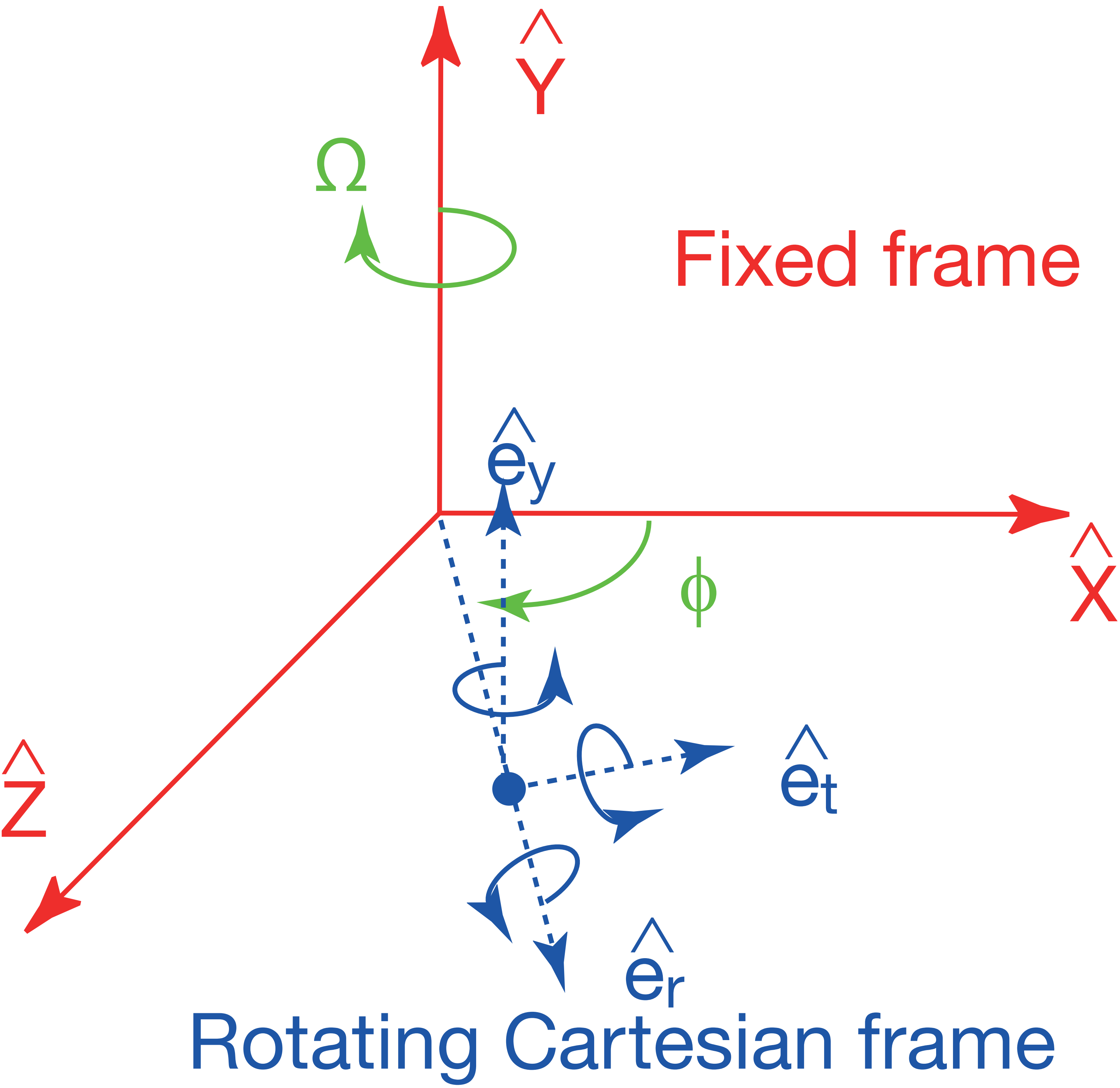

$\hat{Y}$
Ω
Fixed frame
$\hat{e}_y$
$\hat{X}$
ϕ
$\hat{e}_t$
$\hat{Z}$
$\hat{e}_r$
Rotating Cartesian frame

Figure5

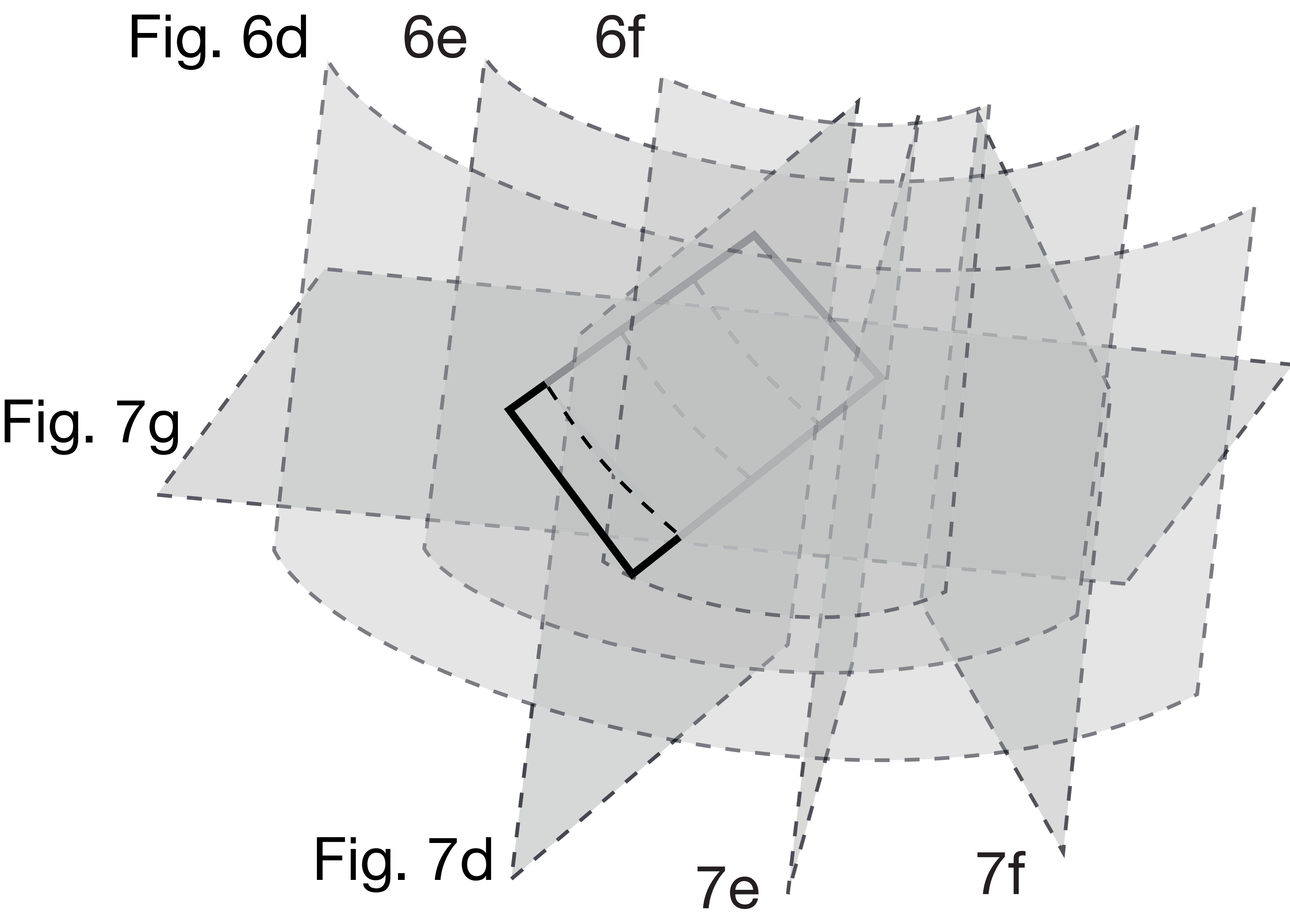

Figure6

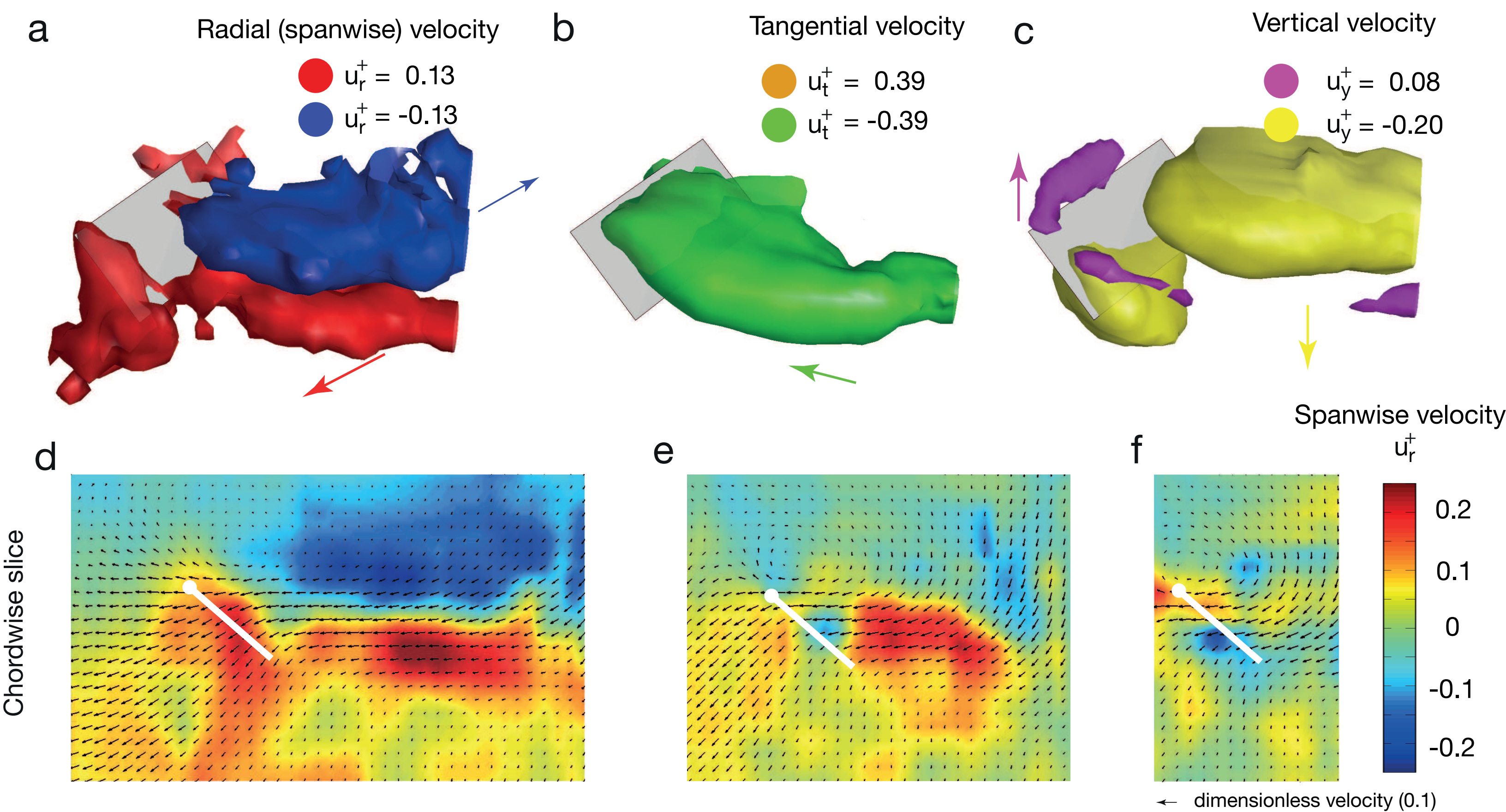

a
Radial (spanwise) velocity
u_r^+ = 0.13
u_r^+ = -0.13
b
Tangential velocity
u_t^+ = 0.39
u_t^+ = -0.39
c
Vertical velocity
u_y^+ = 0.08
u_y^+ = -0.20
d
e
f
Chordwise slice
Spanwise velocity
u_r^+
0.2
0.1
0
-0.1
-0.2
dimensionless velocity (0.1)

Figure7

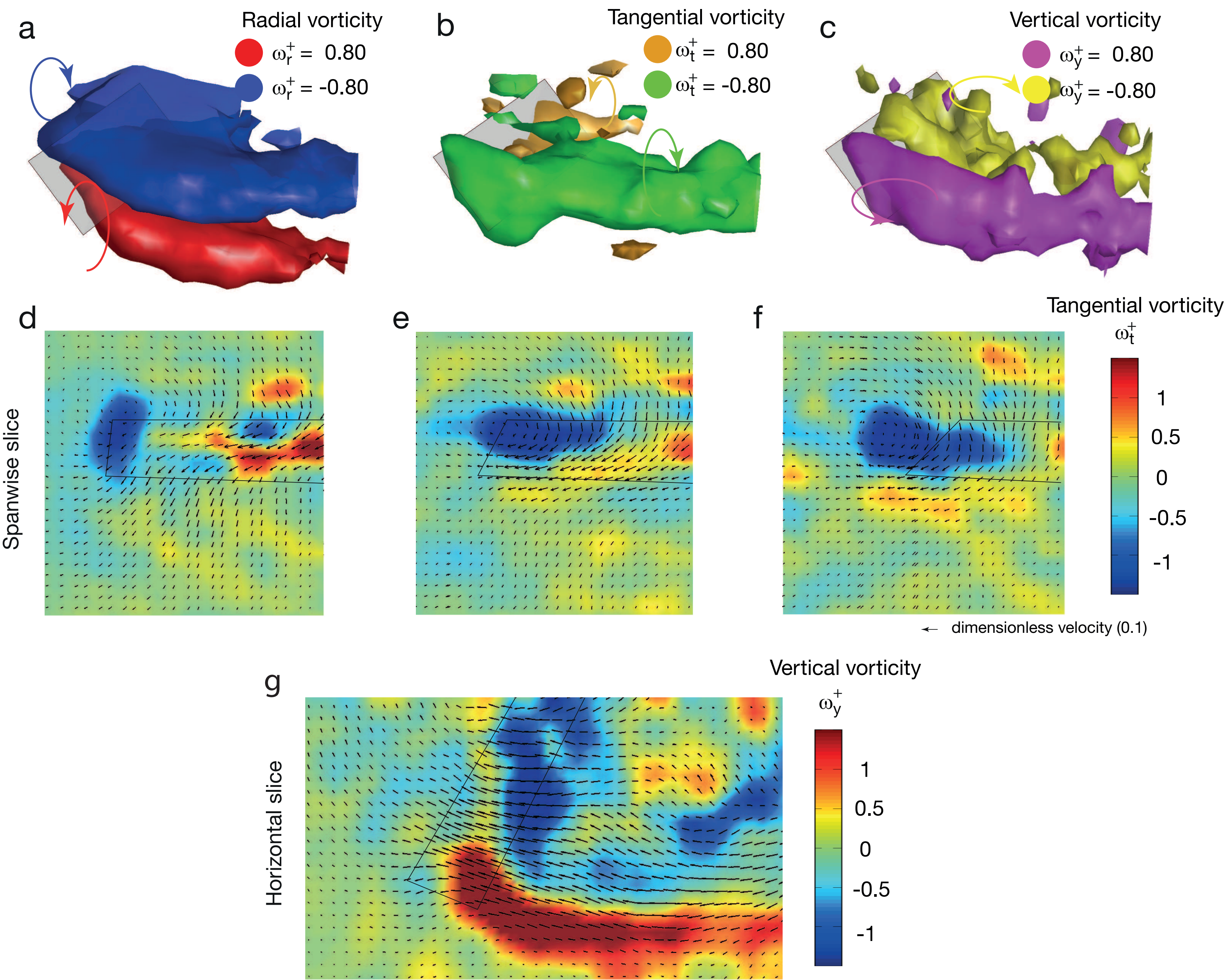

a
Radial vorticity
ω_r^+ = 0.80
ω_r^+ = -0.80
b
Tangential vorticity
ω_t^+ = 0.80
ω_t^+ = -0.80
c
Vertical vorticity
ω_y^+ = 0.80
ω_y^+ = -0.80
d
e
f
Spanwise slice
Tangential vorticity
ω_t^+
1
0.5
0
-0.5
-1
dimensionless velocity (0.1)
g
Horizontal slice
Vertical vorticity
ω_y^+
1
0.5
0
-0.5
-1

Figure8

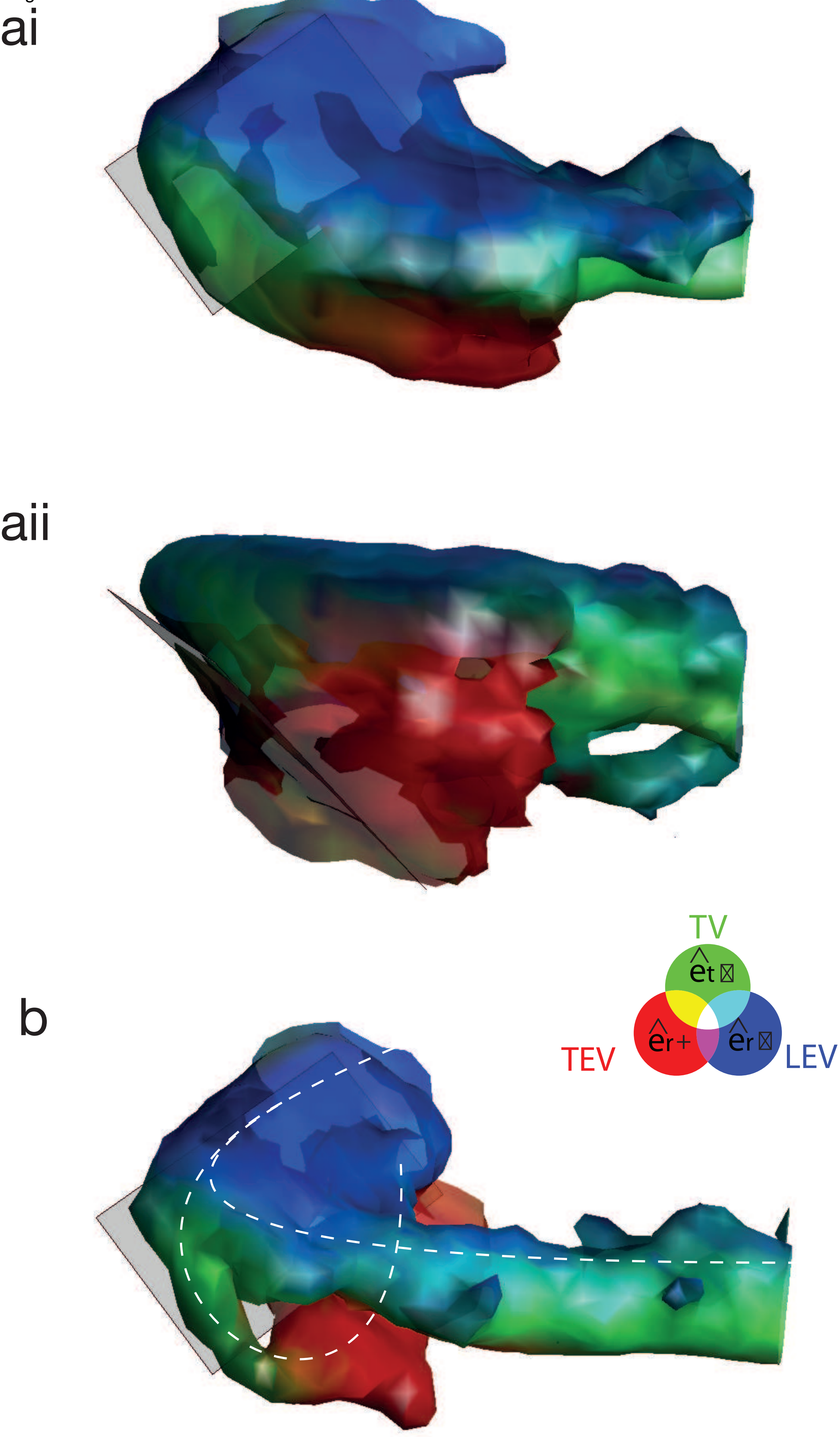

Figure9

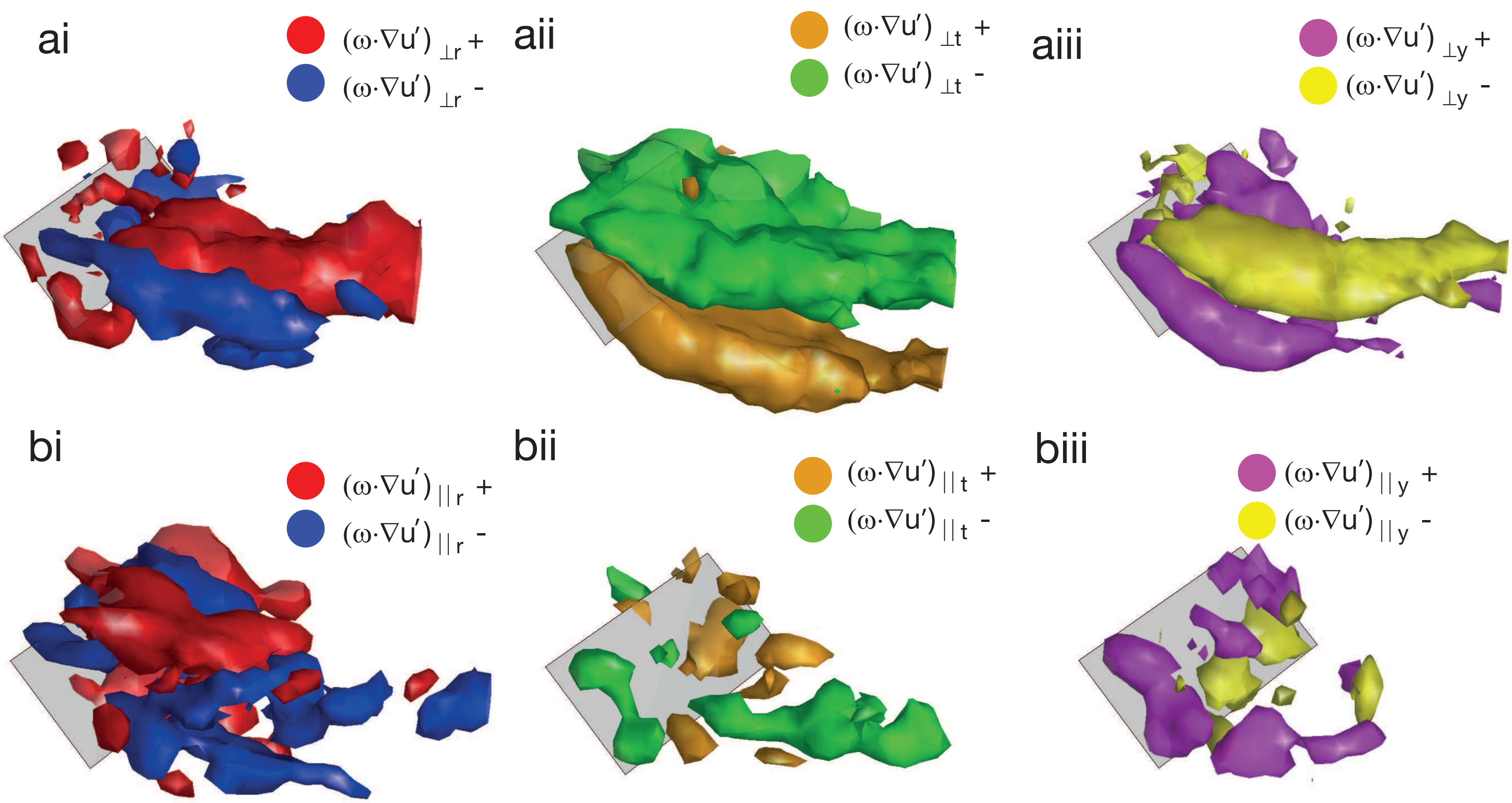
ai
(ω·∇u′) ⊥r +
(ω·∇u′) ⊥r -
aii
(ω·∇u′) ⊥t +
(ω·∇u′) ⊥t -
aiii
(ω·∇u′) ⊥y +
(ω·∇u′) ⊥y -
bi
(ω·∇u′) ||r +
(ω·∇u′) ||r -
bii
(ω·∇u′) ||t +
(ω·∇u′) ||t -
biii
(ω·∇u′) ||y +
(ω·∇u′) ||y -

Figure10

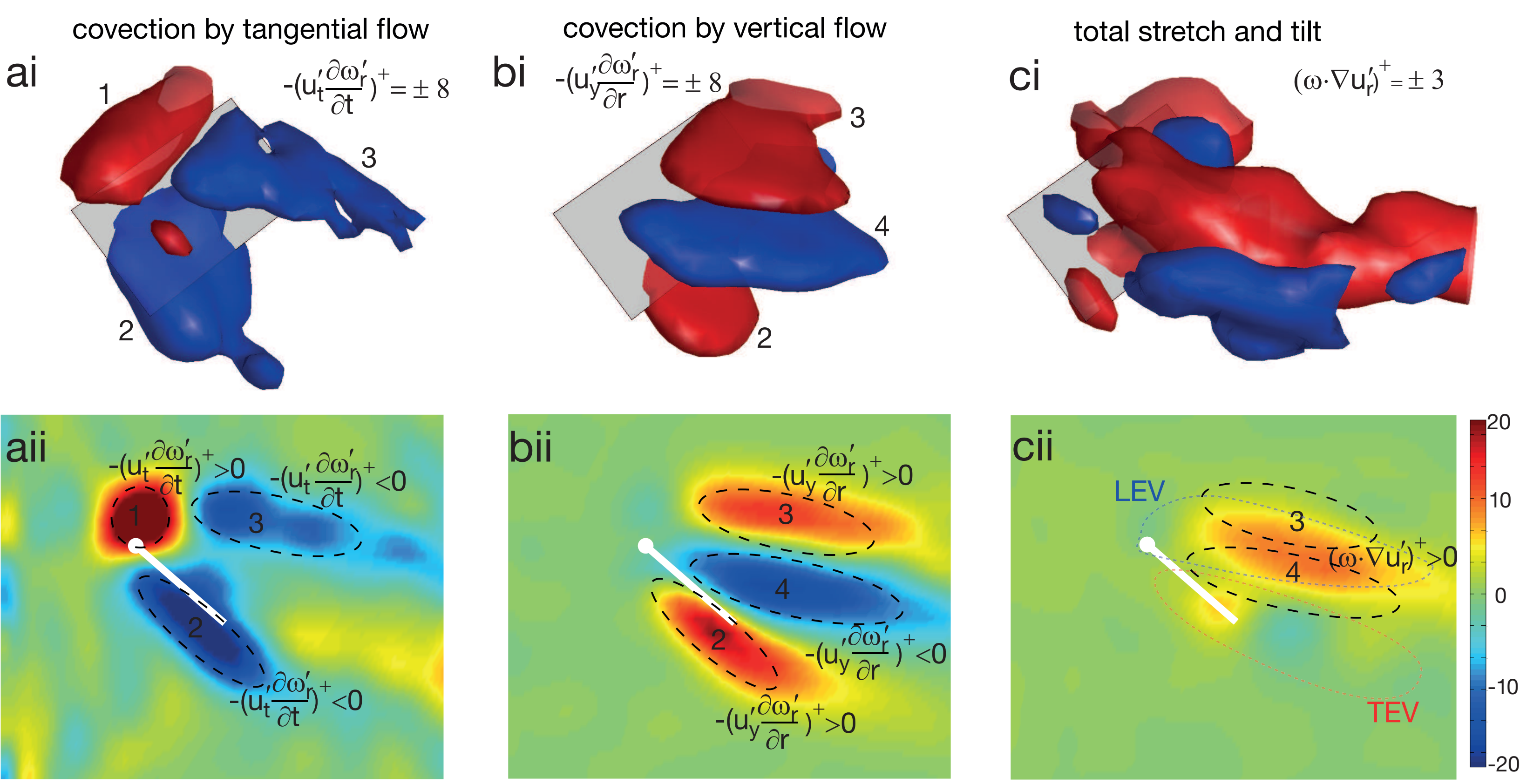

covection by tangential flow
covection by vertical flow
total stretch and tilt
ai
$-(u_t'\frac{\partial \omega_r'}{\partial t})^+ = \pm 8$
1
2
3
bi
$-(u_y'\frac{\partial \omega_r'}{\partial r})^+ = \pm 8$
3
4
2
ci
$(\omega \cdot \nabla u_r')^+ = \pm 3$
aii
$-(u_t'\frac{\partial \omega_r'}{\partial t})^+ > 0$
$-(u_t'\frac{\partial \omega_r'}{\partial t})^+ < 0$
$-(u_t'\frac{\partial \omega_r'}{\partial t})^+ < 0$
1
3
2
bii
$-(u_y'\frac{\partial \omega_r'}{\partial r})^+ > 0$
$-(u_y'\frac{\partial \omega_r'}{\partial r})^+ < 0$
$-(u_y'\frac{\partial \omega_r'}{\partial r})^+ > 0$
3
4
2
cii
LEV
TEV
3
4
$(\omega \cdot \nabla u_r')^+ > 0$
20
10
0
-10
-20

Figure11

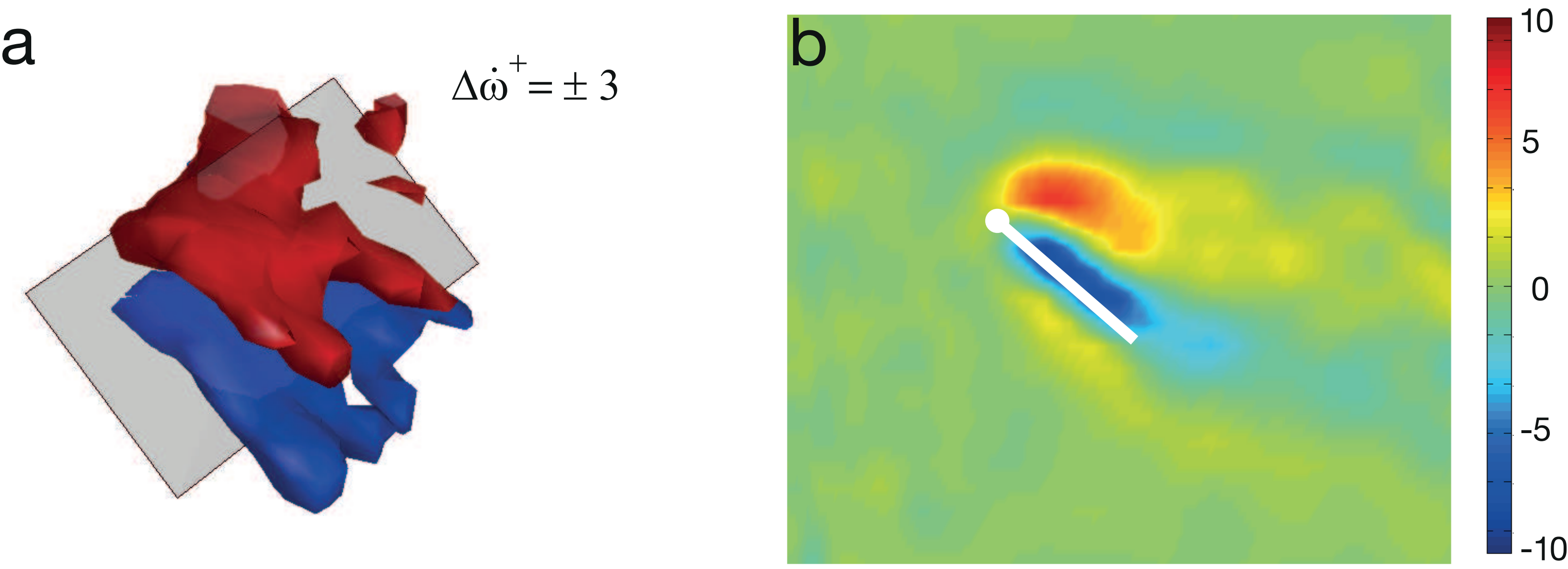

Figure12